The Astrophysical Journal, 738:191 (14pp), 2011 September 10 doi:10.1088/0004-637X/738/2/191
© 2011. The American Astronomical Society. All rights reserved. Printed in the U.S.A.

IMPULSIVE ACCELERATION OF CORONAL MASS EJECTIONS. I. STATISTICS AND CORONAL MASS EJECTION SOURCE REGION CHARACTERISTICS

B. M. Bein[1], S. Berkebile-Stoiser[1], A. M. Veronig[1], M. Temmer[1], N. Muhr[1], I. Kienreich[1], D. Utz[1], and B. Vršnak[2]
[1] IGAM/Institute of Physics, University of Graz, Universitätsplatz 5, 8010 Graz, Austria
[2] Hvar Observatory, Faculty of Geodesy, University of Zagreb, Kačićeva 26, HR-10000 Zagreb, Croatia
Received 2011 March 22; accepted 2011 July 1; published 2011 August 25

ABSTRACT

We use high time cadence images acquired by the *STEREO* EUVI and COR instruments to study the evolution of coronal mass ejections (CMEs) from their initiation through impulsive acceleration to the propagation phase. For a set of 95 CMEs we derived detailed height, velocity, and acceleration profiles and statistically analyzed characteristic CME parameters: peak acceleration, peak velocity, acceleration duration, initiation height, height at peak velocity, height at peak acceleration, and size of the CME source region. The CME peak accelerations we derived range from 20 to 6800 m s^{-2} and are inversely correlated with the acceleration duration and the height at peak acceleration. Seventy-four percent of the events reach their peak acceleration at heights below 0.5 $R_\odot$. CMEs that originate from compact sources low in the corona are more impulsive and reach higher peak accelerations at smaller heights. These findings can be explained by the Lorentz force, which drives the CME accelerations and decreases with height and CME size.

Key words: methods: statistical – Sun: coronal mass ejections (CMEs)

Online-only material: animations, color figures

1. INTRODUCTION

Coronal mass ejections (CMEs) are sporadic ejections of magnetized plasma from the Sun with masses on the order of 10^{13}–10^{16} g (Vourlidas et al. 2010) and velocities in the range of ∼100–3000 km s^{-1} (e.g., Yashiro et al. 2004; Gopalswamy et al. 2009). They are accelerated by magnetic forces in the solar corona and move outward into interplanetary space where they may severely influence the space weather near Earth.

Several case studies of CME kinematics (Gallagher et al. 2003; Zhang et al. 2001, 2004; Maričić et al. 2004; Temmer et al. 2008, 2010) have shown that CMEs typically undergo three phases: a gradual evolution, a fast acceleration, and a propagation phase (Zhang et al. 2001). In the gradual phase, the CME leading edge rises slowly with velocities of some 10 km s^{-1}. At a certain height, the CME undergoes a strong acceleration. How fast and how long the acceleration is varies between events. After the main impulsive acceleration phase the CME propagates at almost constant velocity or shows a gradual acceleration/deceleration due to interaction with the ambient solar wind flow during propagation in the interplanetary space (e.g., Gopalswamy et al. 2000).

Recent studies suggest that the main acceleration of impulsive CMEs occurs at low coronal heights, which are not observable in traditional white light coronagraphic images (Gallagher et al. 2003; Temmer et al. 2008, 2010). Thus, if we are interested in the origin of CMEs and their initial acceleration, we have to observe them from their initiation site close to the solar surface. To observe fast CME accelerations, it is important to have image sequences with high time cadence during this important dynamical phase. Since fast and impulsive events severely contribute to our space weather, they are particularly relevant to study.

Acceleration measurements of the early phase of CME propagation for a statistical sample of 50 events were performed by Zhang & Dere (2006) who used coronagraphic observations from 1.1 $R_\odot$ to 30 $R_\odot$ (LASCO C1, C2, and C3) before the LASCO C1 coronagraph failed in 1998 due to communication loss with the *SOHO* spacecraft. Vršnak et al. (2007) combined EUV images (*SOHO* EIT) with coronagraphic observations (MLSO Mark-IV K, LASCO C2 and C3) in order to track CMEs from their initiation site up to about 30 $R_\odot$. They analyzed a sample of 22 events, which contain predominantly gradual CMEs.

For our study, we used *STEREO* (Kaiser et al. 2008) data that provide high time cadence EUV imaging and coronagraphic observations up to 15 $R_\odot$ with an overlapping field of view (FOV). Based on this data set, we derived detailed CME kinematics and acceleration profiles for a sample of 95 impulsive CME events that occurred during 2007 January and 2010 May, representing the largest data set for the study of impulsive CME acceleration so far. In this paper, statistics and correlation analysis of the kinematical and dynamical CME characteristics are presented. In our parameter study, we focus on the CME peak velocity, peak acceleration, acceleration duration, height at peak velocity, height at peak acceleration, initiation height, and the CME source region size. The relation of the CME characteristics to the associated flare, filament eruption, large-scale EUV waves, and magnetic topology will be presented in a forthcoming paper.

2. DATA AND DATA REDUCTION

The SECCHI package (Howard et al. 2008) on board the twin *STEREO* spacecraft, *STEREO-A* (ahead) and *STEREO-B* (behind), includes an Extreme Ultraviolet (EUV) Imager (EUVI; Wuelser et al. 2004), two white light coronagraphs (COR1 and COR2), and two white light heliospheric imagers (HI1 and HI2), observing the Sun in different FOVs. We combined data from EUVI, COR1, and COR2, in order to study the kinematics of CMEs from their initiation close to the solar surface up to a distance of about 15 $R_\odot$. EUVI observes the solar chromosphere and low corona in four different wavelengths in an FOV up to 1.7 $R_\odot$. To track a CME, we mostly used images

in the 171 Å passband because of the high time cadence up to 75 s, but in some cases it was only possible to track the CME in the 195 Å observations, which on average have a lower time cadence (for most events 10 minutes, but in some cases as good as 2.5 minutes). The high time cadence enabled us to obtain detailed acceleration profiles especially at the beginning of the CME propagation.

The two *STEREO* coronagraphs, COR1 and COR2, observe the inner and outer solar coronae in an FOV of 1.4 to 4 $R_\odot$ and 2.5 to 15 $R_\odot$, respectively. The overlapping FOVs of all three instruments enabled us to connect the same structure in the observations by the different instruments. The time cadence of the COR1 observations is mainly 5 minutes but can be up to 20 minutes in some cases, the cadence of COR2 is 30 minutes.

We started our study with a sample of 146 selected CME events. For our selection, we preferred events that could already be observed in the low corona (i.e., by the EUVI instrument), in order to gain insight into the early phase of CME dynamics. In addition, we required that the source region of a CME could be identified on the visible solar hemisphere, for which we used the location of associated flares as an additional marker. All events do not fulfill both requirements (99 events could be measured in the EUVI FOV, for 89 events a flare could be associated). In most cases the associated flares were weak. Five events were associated with an M class flare and 26 CMEs were associated with a C class flare. The remaining flares were of GOES class B or below.[3] The final CME sample for the statistics presented in this paper comprises a set of 95 events, for which we could derive the full CME acceleration profile, i.e., the peak acceleration and the acceleration duration could be measured for each CME. Eighty-four of them were tracked starting from the EUVI FOV.

All data were reduced by the SECCHI solar software routine `secchi_prep`. The EUVI image sequences were corrected for differential rotation, and for weak events a normalizing-radial-graded filter (Morgan et al. 2006) was used. For the COR1 and COR2 observations a pre-event image was subtracted. In addition, a sigma filter and a normalization technique were applied to get better contrasts on the transient faint CME structures. For the measurements of CME evolution, running difference and running ratio images were reconstructed.

3. METHODS AND ANALYSIS

We derived the CME kinematics by measuring the position of the CME leading edge in EUVI, COR1, and COR2 images. In order to obtain reliable and reproducible measurements, an algorithm was developed which semi-automatically determines the position of the CME leading edge in EUVI, COR1, and COR2 running difference images. The leading edge of a CME appears as a bright front with a sharp intensity drop to regions outside the CME. This information is the basis for the algorithm developed to quasi-automatically identify the CME leading edge and its evolution in subsequent images. The algorithm works in the following way: the running difference images are contoured with brightness levels starting at very low, positive intensities. Then the distances of the pixels on the outermost contour with respect to the Sun's center are calculated. This process is repeated with contours at incrementally increasing brightness levels until the mean distance derived from two subsequent contour levels is separated by a sufficiently small, prescribed distance between each other. The position of the last determined contour is supposed to provide the location of the CME leading edge. The result can be manually corrected if necessary (e.g., if image artifacts are included in the contour, or if the CME front is not well defined). We note that faint CMEs were mostly measured by visual identification of the CME leading edge since the algorithm fails here. Figures 1 and 2 show examples of EUVI, COR1, and COR2 running difference image sequences of two well-observed CMEs, where the identified CME leading edge and the determined propagation direction are indicated. We assumed a propagation along a straight line and defined for each event a direction, which crosses the outermost part of the CME front. The CME distance was derived by following the evolution of the identified CME leading edge along this main propagation direction. In a few cases, a linear propagation could not be assumed due to deflection toward the heliospheric current sheet. For these events, the outermost part of the measured CME leading edge was manually selected in each frame. The distance was averaged over an angular extent of 10° of the determined leading edge and measured from the CME source region, which allows us to follow the CME propagation even if it deviates from the radial direction.

There are several factors affecting the determination of the CME leading edges and several possible sources for systematic errors. On the one hand, the CME itself can change its appearance with time, e.g., the front might become blurred which makes it difficult to track the same feature over several solar radii. On the other hand, we combine observations of different instruments with different angular resolution and the detection sensitivity varies over the FOV. In addition, stray light levels are different for COR1 and COR2, influencing the appearance of the observed white light feature. In order to estimate the average error included in our kinematical measurements, we analyzed some selected CMEs in detail. For each of these events, we followed the tracked CME leading edge in time in EUVI, COR1, and COR2 images four times. For each run, the scaling of the images was chosen differently, in order to account for the different visibilities of the outer (fainter) CME features. From the thus obtained height–time measurements, we derived the mean and standard deviation at each instant from the different measurement runs. The results from this procedure suggest an average error of 0.03 $R_\odot$ for measurements in EUVI, 0.125 $R_\odot$ in COR1, and 0.3 $R_\odot$ in COR2 data, respectively.

Numerical differentiation of the height–time curve provides the CME velocity and acceleration profiles as a function of time. Due to the fact that errors in the height–time curve are enhanced by the first and second derivatives, a smoothing and fitting method is used. We used a spline fitting procedure in which the measured CME height–time profile is subdivided into consecutive segments. All segments are then fitted by cubic splines and at their end points ("nodes"), the functions merge continuously and are twice continuously differentiable. The user input for the fitting procedure is the number and positions of nodes. The spline-fitted curve is then used as the basis for deriving the velocity and acceleration evolution by subsequent numerical differentiation. In the course of fitting, we also estimated errors for the velocity and acceleration for each of the fitted segments. For each segment, the uncertainties on the polynomial spline coefficients are derived. The errors on the velocity and acceleration were then determined via Gaussian error propagation.

The advantage of using this method is that it provides reasonable errors (especially for the acceleration) also in cases

[3] We note that the CME events in this study occurred during the extreme solar minimum period (2007–2010), which explains the lack of associated high-energy flare events.

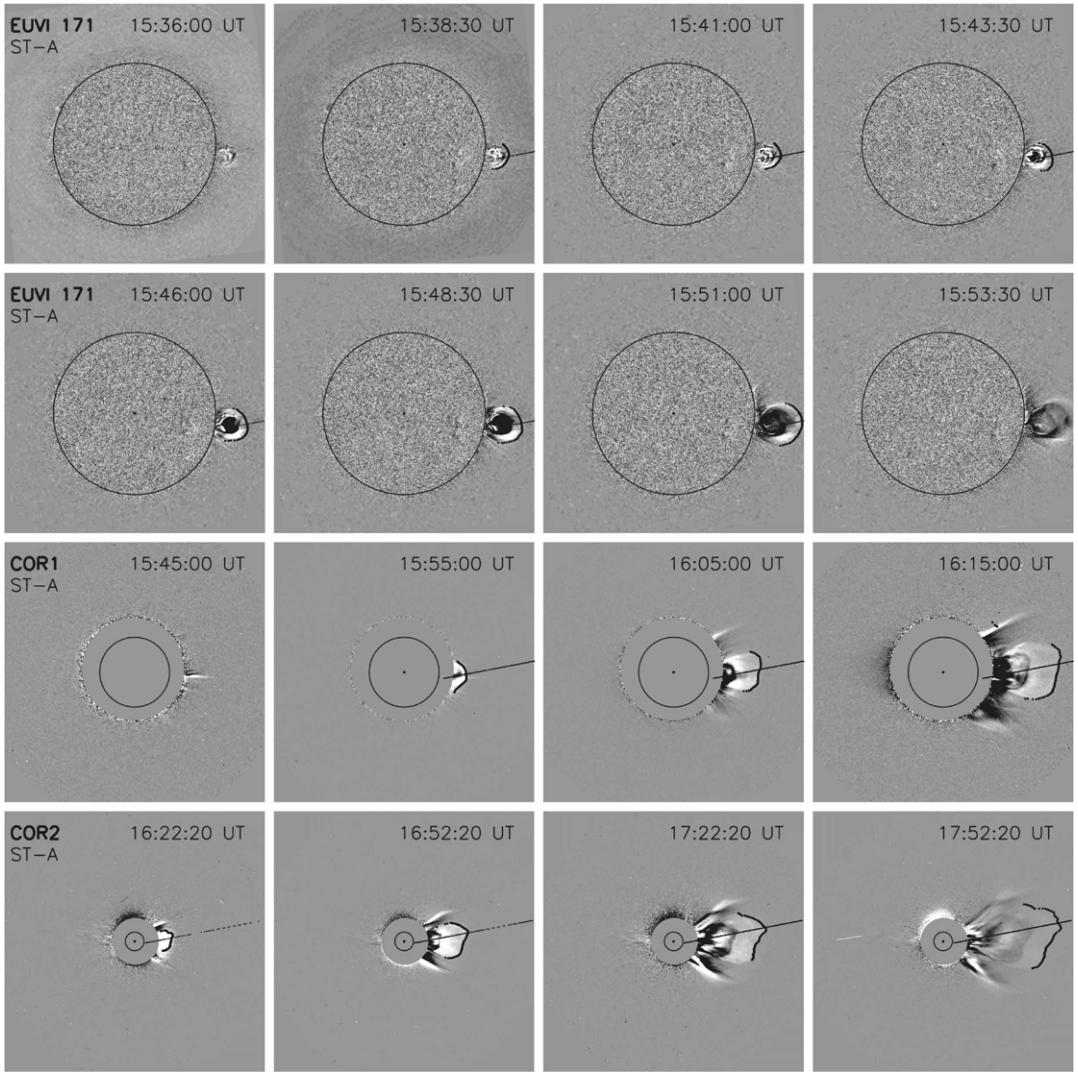

Figure 1. Time sequence of EUVI 171 Å (first and second rows), COR1 (third row), and COR2 (bottom row) images of the CME observed on 2008 April 5 by *STEREO-A*. The curved line marks the identified CME leading edge and the straight line indicates the propagation direction. The CME kinematics derived for this event is plotted in Figures 5 and 8. All EUVI images are plotted in an x-range of [−1600″, +1600″] and in a y-range of [−1470″, +1730″]; the selected COR1 range for both directions is [−3720″, +3720″] and the COR2 range [−14 000″, +14 000″]. Note that not all images available are shown.

(An animation of this figure is available in the online journal.)

of high time cadence, where the classical error estimates using two neighboring points yield typically very high errors for the CME accelerations. Different sets of nodes giving similar fits for a certain height–time curve may reveal considerably different velocity and acceleration profiles (for details see the appendix in Vršnak et al. 2007). A fit was preferred over the other if the errors in velocity and acceleration were smaller, which basically confined the number of nodes to 5–7.

To estimate the CME source region size, we used different methods, described in detail in Vršnak et al. (2007): (1) the distance between bipolar coronal dimming regions derived from EUVI 195 Å or 171 Å observations, (2) the footpoint separation of the associated eruptive filament/prominence observed in EUVI 304 Å images, (3) the lengths of the flare ribbon brightenings observed in the chromosphere or transition region measured in EUVI 304, 171, or 195 Å images.

4. RESULTS

In this paper, a statistical analysis of 95 impulsive CME events is presented. For 90 of these events a source region could be uniquely determined. Figure 3 shows their positions on the solar disk. Most of the events studied occurred close to the solar limb, and thus the influence of projection effects is small. Figure 3 also reveals the transition from solar cycle No. 23 to No. 24, with the CME source regions changing from locations close to the equator at the end of cycle No. 23 to higher latitudes for CMEs already belonging to cycle No. 24. Figure 4 shows the distribution of the projected radial distance of the CME source regions to Sun center in units of $R_\odot$. A clear peak at 0.9–1 $R_\odot$ can be seen, which includes 49 events (more than 51%). Only 21% have distances smaller than 0.7 $R_\odot$, and only one event occurred close to the disk center.

In Figures 1 and 2 we show EUVI and COR image sequences of two sample CMEs from our data set. The two events occurred on 2008 April 5 and 2007 May 23, respectively, and could be well observed in all three instruments: EUVI, COR1, and COR2. In both cases 16 representative images are selected; the entire evolution of events can be seen in the accompanying movies. In each running difference image, the solar limb is overplotted and the identified CME leading edges are marked. We measured the CME propagation along a straight line (also plotted in the image)

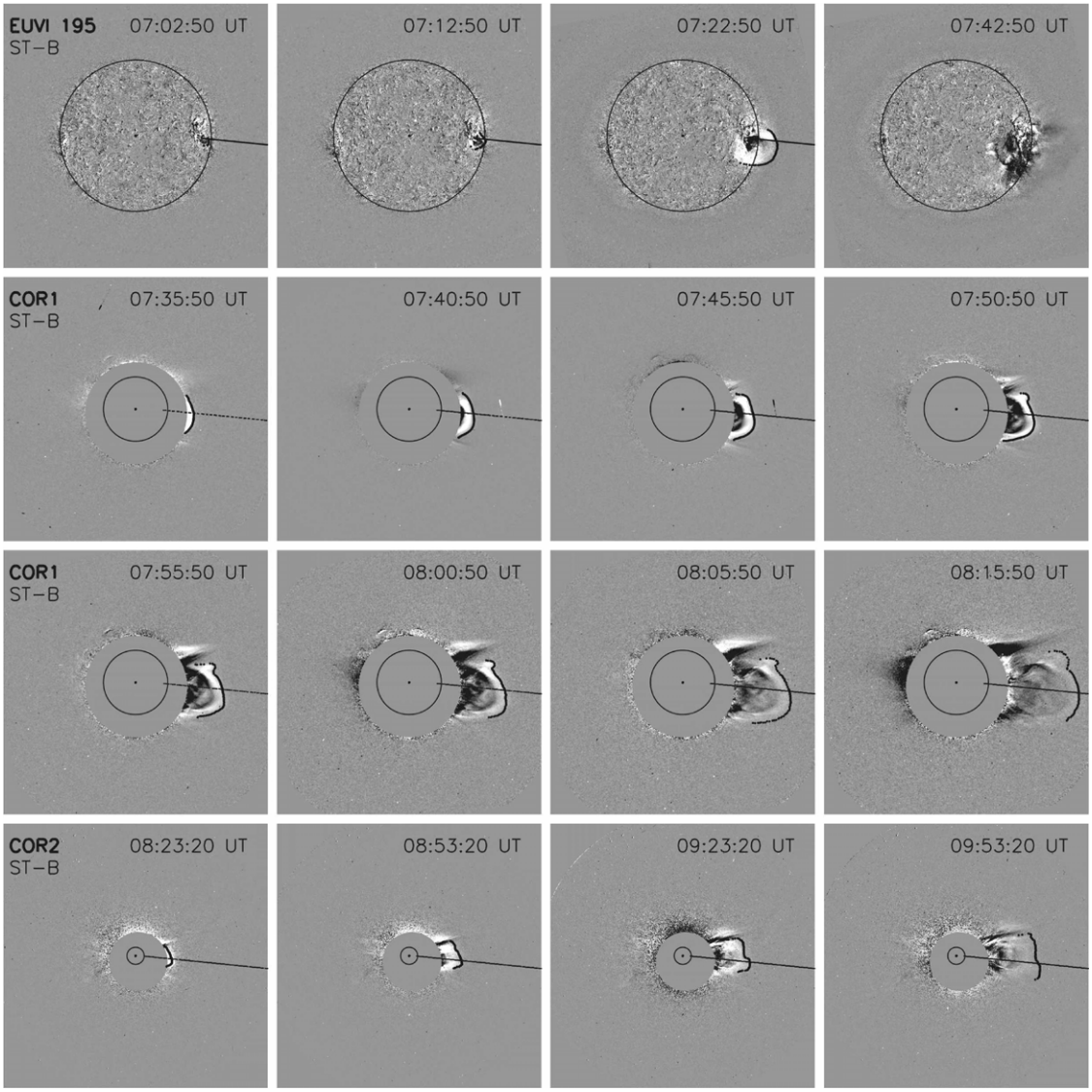

Figure 2. Same as Figure 1 but for the CME event observed on 2007 May 23 by *STEREO-B*. The CME kinematics derived for this event are plotted in Figures 6 and 8. The ranges in the *x*- and *y*-directions are [−1580″, +1580″] for EUVI 195 Å, [−3720″, +3720″] for COR1, and [−14 000″, +14 000″] for COR2.

(An animation of this figure is available in the online journal.)

that originates at the CME source region. In both examples, the observed CMEs change their shape during their propagation until they reach the end of the COR2 FOV. Selected images from the different instruments, which observed the CME almost simultaneously, were overlaid to check if we really observed the same structure. This was possible, for example, for the EUVI image taken at 15:53:30 UT and the COR1 image taken at 15:55:00 UT in Figure 1.

The kinematical plots derived for the CMEs shown in Figures 1 and 2 as well as for four more CME events from our sample can be seen in Figures 5–7. The upper two rows of panels show the CME height, the middle row shows the velocity, and the bottom row shows the acceleration evolution over time. Although all six events show the typical three-phase kinematical behavior (gradual initiation, acceleration, and propagation phase), their kinematics reveal distinct differences. The event observed on 2009 February 13 (Figure 7) shows a very strong ($a_{\rm max}$ ∼970 m s^{-2}) and short acceleration phase of 9 minutes, whereas the events that occurred on 2008 November 6 (Figure 6) and 2007 May 23 (Figure 7) exhibit long acceleration durations of 50 and 72 minutes, respectively, with peak accelerations of ∼400 m s^{-2} and ∼280 m s^{-2}. For the event observed on 2010 May 5 (Figure 5) an acceleration of 29 minutes and the smallest peak acceleration ($a_{\rm max}$ ∼250 m s^{-2}) of the six events shown in Figures 5–7 were measured. The remaining two events plotted in Figure 6 (2008 April 5 and 2007 May 8) reveal peak accelerations of 850 m s^{-2} and 690 m s^{-2} and acceleration durations of 26 minutes and 17 minutes, respectively.

Figure 8 shows for the six events plotted in Figures 5–7 the CME velocity and acceleration profiles against height together with the error ranges derived from the spline fits. Differences are remarkable, in particular at which height the peak acceleration takes place. The event observed on 2008 November 6 reaches its maximum acceleration at a height of 0.84 $R_\odot$ above the CME source region, whereas for the other five events the height at peak acceleration is distinctly lower. For instance, the event observed on 2007 May 23 was at a height of 0.12 $R_\odot$ above the CME source region when it reached its peak acceleration of 280 m s^{-2}.

For each CME we derived several characteristic parameters: (1) peak velocity $v_{\rm max}$, (2) peak acceleration $a_{\rm max}$, (3) acceleration duration $t_{\rm acc}$, (4) height at peak velocity $h_{\rm vmax}$, (5) height at

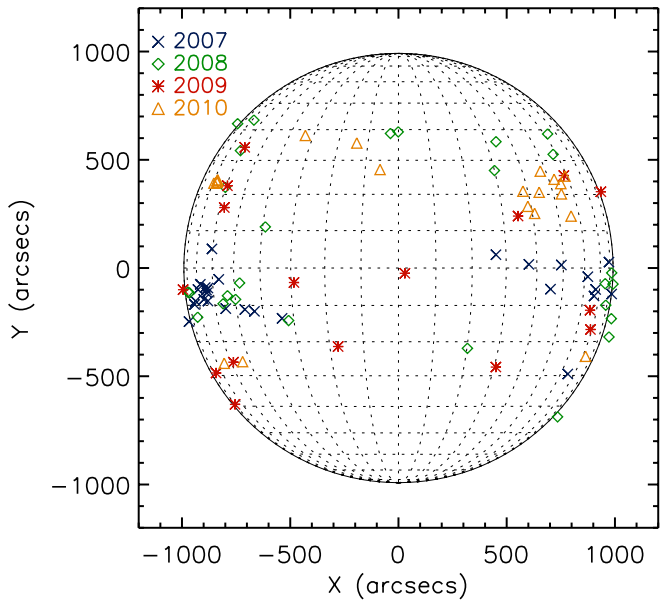

Figure 3. Positions of the CME source regions on the solar disk as observed from the actual *STEREO* vantage points. Different colors and symbols represent the different years of occurrence during the minimum phase of solar cycle No. 23/24.

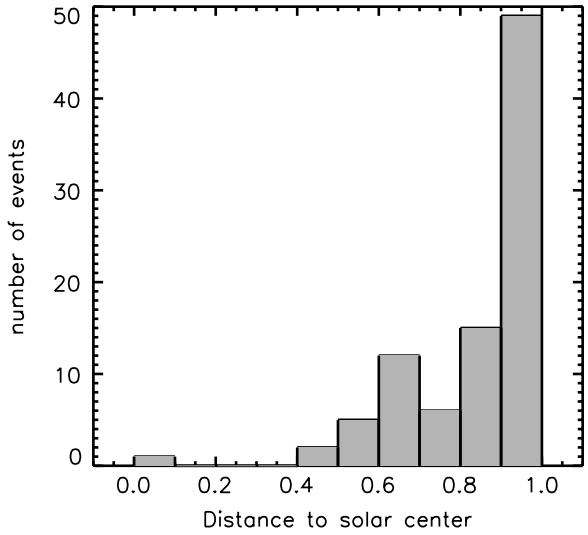

Figure 4. Distribution of the projected radial distances of the CME source regions from Sun center in units of $R_\odot$ with a bin size of 0.1 $R_\odot$.

peak acceleration h_{amax}, (6) first height measured h_0, (7) source region size L.

The peak velocity v_{max} and peak acceleration a_{max} were derived from the spline fit of the velocity–time curve and the acceleration–time curve, respectively (see middle and bottom rows of panels in Figures 5–7). The measured velocity at the end of the COR2 FOV ($\sim$15 $R_\odot$) could result from the combination of two different effects, the main and the residual acceleration. If the residual acceleration is positive, the CME velocity profile peaks later but if the residual acceleration is negative, the maximum velocity is reached at the end of the main acceleration phase. The residual acceleration can be positive for two reasons. On the one hand, in slow and gradual events the ambient solar wind flow causes a further acceleration. On the other hand, it is also possible that the CME accelerates continuously due to continuous energy release after the main phase (e.g., Cheng et al. 2010). Since we are interested in the CME velocity corresponding to the main acceleration phase, we determined v_{max} as that value of the CME velocity when the CME acceleration has decreased to 10% of its peak value.

The acceleration duration $t_{\mathrm{acc}} = t_{\mathrm{acc\_end}} - t_{\mathrm{acc\_start}}$ was extracted from the acceleration profile, where $t_{\mathrm{acc\_start}}$ and $t_{\mathrm{acc\_end}}$ were defined as the times when the CME acceleration profile is again at the 10% level of the peak value. The height at peak velocity h_{vmax} and the height at peak acceleration h_{amax} were derived from the velocity and acceleration profiles against the height (see Figure 8), h_{vmax} being related to the 10% level of a_{max}. The height h_0 at which the CME was first observed can be understood as a rough estimate of the height of CME initiation, since we observed all CMEs from their origin in the low corona.

The top panel of Figure 9 shows the distribution of the CME peak velocities. We found a range for v_{max} from 56 to 1279 km s^{-1} with a mean value of 526 km s^{-1} and a median of 460 km s^{-1}. The mode of the distribution lies at 300–400 km s^{-1}. In comparison, Vršnak et al. (2007) measured 22 CMEs, which occurred in a period between 2002 February and 2005 January, i.e., the maximum and decay phase of solar cycle No. 23, covering a range of 365–2775 km s^{-1} with a mean value of 940 km s^{-1}. These linear velocity values are higher than the CME peak velocities in our study, which covers only events that occurred during the extreme solar minimum. Indeed, Gopalswamy et al. (2009), who derived the linear velocity for about 11000 LASCO CMEs that occurred between 1996 and 2006, found that the mean velocity values vary from 300 to 600 km s^{-1} during the solar cycle with an average value of 475 km s^{-1} for the whole sample.

The distribution of the CME peak velocities v_{max} derived in our study is asymmetrical with a tail toward high velocity values. This coincides with the findings of Yurchyshyn et al. (2005) for the distribution of the linear velocity of 4315 CMEs, which was fitted by a lognormal fit. The lognormal probability density function derived from our sample of v_{max} is overplotted in Figure 9 (top panel) as a solid line. Mathematically, an independent variable x is lognormally distributed when its natural logarithm, $\ln(x)$, matches a normal distribution. A normal distribution is created by the sum of independent variables, whereas a lognormal distribution is created by the product of independent variables. In other words, if a variable is lognormally distributed, this hints at a multiplication of independent physical processes underlying the distribution (Limbert et al. 2001; Yurchyshyn et al. 2005). The probability function $f(x)$ of the lognormal distribution can be written as

$$f(x) = \frac{1}{\sqrt{2\pi}\sigma x} \exp\left(-\frac{(\ln(x)-\mu)^2}{2\sigma^2}\right), \qquad (1)$$

where μ is the mean and σ is the standard deviation of the natural logarithm of x. With reference to Limbert et al. (2001) we use $\mu^* = e^{\mu}$ and $\sigma^* = e^{\sigma}$ as the median and the multiplicative standard deviation. Thus, the confidence interval of 68.3% is given as $[\mu^*/\sigma^*, \mu^* \cdot \sigma^*]$. From the lognormal fit to the v_{max} distribution (Figure 9, top panel) we obtained $\mu = 6.09$ and $\sigma = 0.47$ corresponding to a median $\mu^* = 441$ km s^{-1} with the bounds of the confidence interval at [276 km s^{-1}, 706 km s^{-1}].

To discover how projection effects influence our results, we plot in Figure 10 the CME peak velocity against the radial distance of the CME source region to the Sun's center. The correlation coefficient of these two parameters is $c = 0.011$, i.e., very low and thus projection effects do not have a significant effect. This is probably due to the fact that a distinct correlation

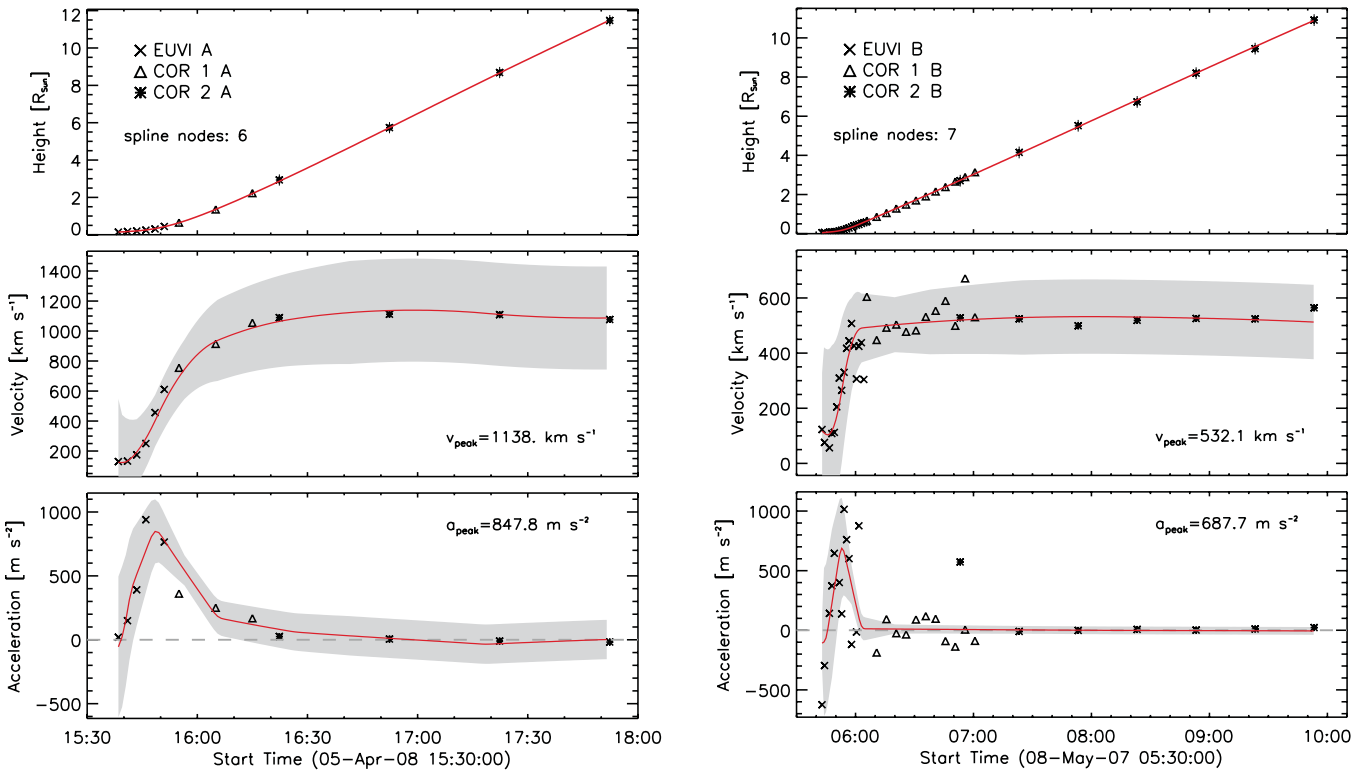

Figure 5. CME kinematics for the events observed on 2008 April 5 (left) and 2007 May 8 (right). The top panels show the height–time curve derived from EUVI (crosses), COR1 (triangles), and COR2 (asterisks) measurements together with the measurement errors. Note that these errors (0.03 $R_\odot$ for EUVI, 0.125 $R_\odot$ for COR1, and 0.3 $R_\odot$ for COR2 measurements) may appear smaller than the plot symbols due to the large height range presented. The solid line represents the spline fit to the height–time curve. The middle and bottom panels show the CME velocity and acceleration profiles derived from numerical differentiation of the CME height–time measurements of the spline fit (solid line). The velocity and acceleration values derived by direct numerical differentiation of the measurement points (symbols) as well as the error range derived from the spline fits (gray-shaded area) are overplotted.

(A color version of this figure is available in the online journal.)

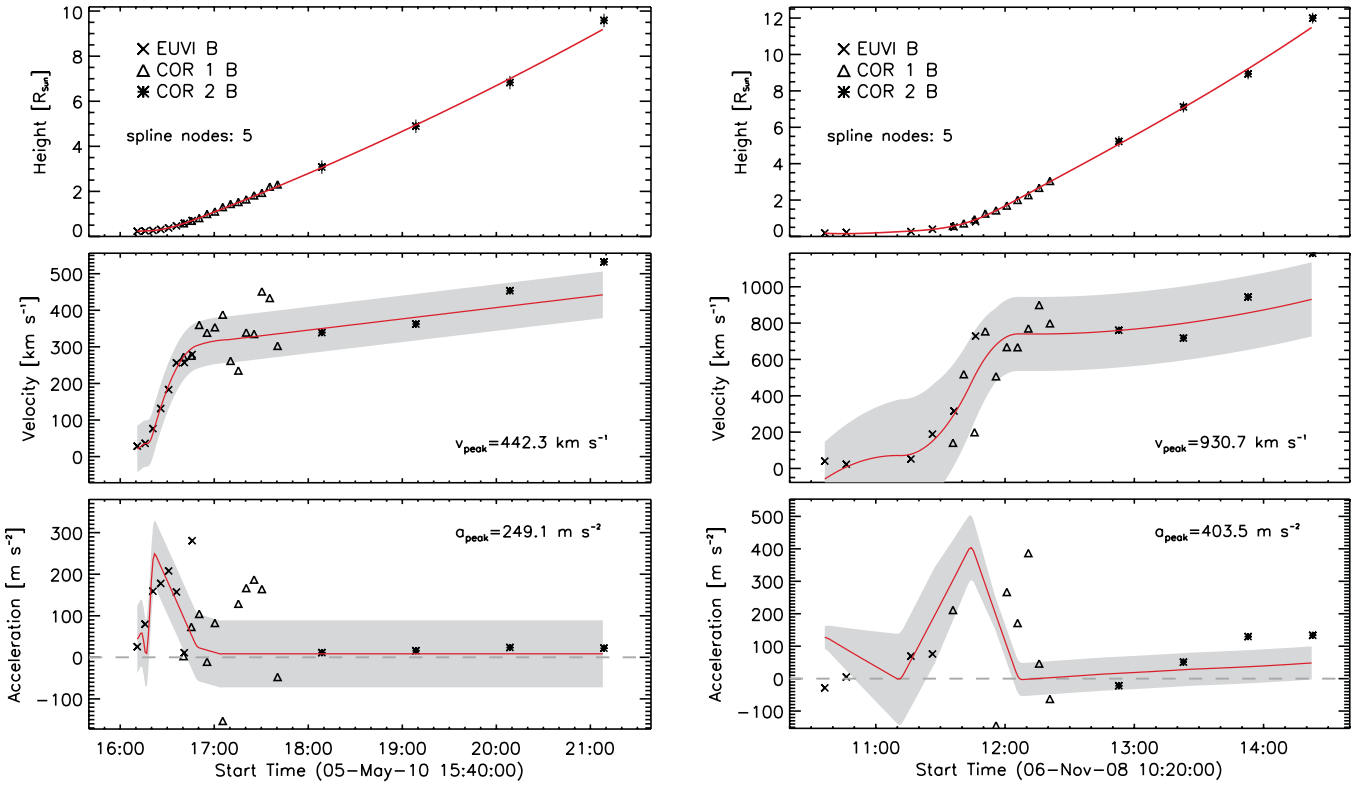

Figure 6. Same as Figure 5 but for the events observed on 2010 May 5 (left) and 2008 November 6 (right).

(A color version of this figure is available in the online journal.)

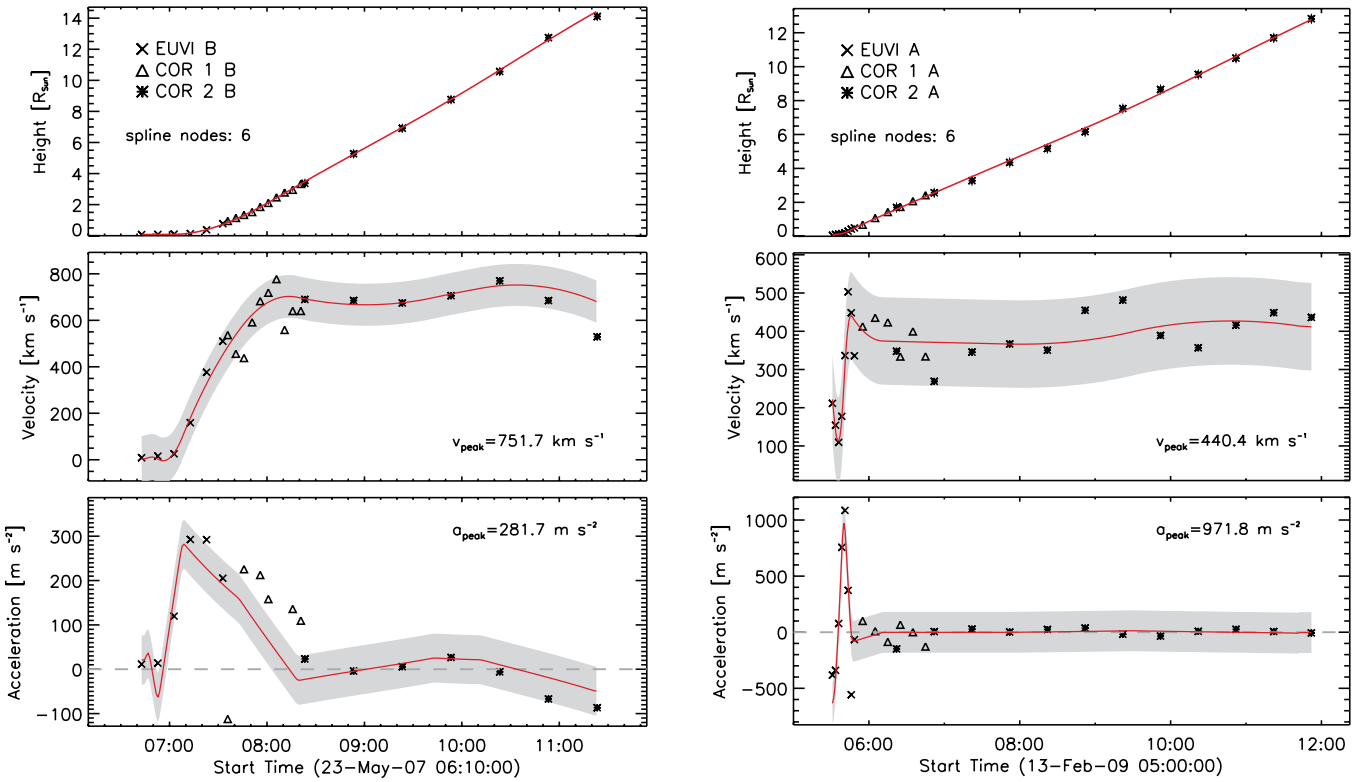

Figure 7. Same as Figure 5 but for the events observed on 2007 May 23 and 2009 February 13.
(A color version of this figure is available in the online journal.)

exists between the CME radial propagation and its lateral expansion (Schwenn et al. 2005). Thus, the effect of projection on the derived CME velocities is much less than could be expected in the case of point sources.

The middle plot of Figure 9 shows the distribution of the CME peak acceleration a_{max} for the whole sample. The a_{max} values cover a wide range between 19 m s^{-2} and 6781 m s^{-2}. Forty percent of the events have a peak acceleration >600 m s^{-2}, 19% show values >1000 m s^{-2}, and five events (observed on 2007 May 30, 2007 June 3 ∼ 06:00 UT, 2007 June 3 ∼ 09:00 UT, 2007 August 17, and 2010 February 12) reached a_{max} values >2000 m s^{-2}. The distribution peak is well-defined at 200–300 m s^{-2}; the mean and median values are 756 m s^{-2} and 414 m s^{-2}, respectively. For the distribution of the CME peak acceleration we again applied a lognormal fit, with the parameters $\mu = 6.09$ and $\sigma = 1.04$ corresponding to a confidence interval of [156 m s^{-2}, 1248 m s^{-2}] around $\mu^* = 441$ m s^{-2}. Since the majority of the a_{max} values are concentrated in the range between 0 and 2000 m s^{-2}, we plotted the detail of the histogram for that range at the bottom of Figure 9.

The large range of a_{max} values (19–6781 m s^{-2}) spreading over two orders of magnitude is similar to former studies from Vršnak et al. (2007), 40–7300 m s^{-2}, and Zhang & Dere (2006), 2.8–4464.9 m s^{-2}. The mean value of a_{max} = 749 m s^{-2} in our study is comparable to the value from Vršnak et al. (2007), 840 m s^{-2}, but more than twice as high as the mean value in the sample of Zhang & Dere (2006), 330 m s^{-2}. It is worth noting that on average the CME peak velocities derived from CMEs that occurred during the extreme solar minimum (present study) are considerably smaller than those during solar maximum studied by Vršnak et al. (2007), but the CME peak accelerations are similar in both samples. This may be an effect of the better time cadence of the *STEREO* instruments which enables us to reconstruct fast changes in the CME kinematics.

The distribution of the acceleration phase duration t_{acc}, which peaks at 20–30 minutes, is shown in Figure 11 together with the lognormal fit. More than 50% of the events have t_{acc} values smaller than 30 minutes; however, we also measured acceleration durations up to 8.6 hr. Only one event (observed on 2008 October 17) has an acceleration duration of >200 minutes. Thus, we show in the bottom panel of Figure 11 a zoom into the range of 0–200 minutes. The smallest value we obtained is 4.5 minutes. The arithmetic mean of 44.6 minutes is considerably lower than the values derived in Vršnak et al. (2007), 120 minutes, and Zhang & Dere (2006), 180 minutes, which indicates that our sample contains mainly impulsive events. The wide range of t_{acc} of three orders of magnitude was also found by Vršnak et al. (2007) and Zhang & Dere (2006). In both of these studies the distribution peaks at 0–50 minutes, consistent with our results. The distribution of t_{acc} was fitted with the lognormal fit parameters $\mu = 3.39$ and $\sigma = 0.79$ which corresponds to a confidence interval of [13.5 minutes, 65.4 minutes] around $\mu^* = 29.7$ minutes.

Figure 12 shows the distributions for the various CME height parameters, h_0, h_{vmax}, and h_{amax}. The distribution for h_0, the height at which the CMEs were first observed, is shown in the top panel of Figure 12. This is a measure for the height above the solar surface at which the CME is initiated. However, we stress that h_0 is not exactly the real CME initiation height but a rough measure for it, since it is affected by (1) projection effects and (2) sensitivity issues, i.e., the measured h_0 is expected to be larger than the real CME initiation height in cases where the CME could not be identified from the very beginning. The measured h_0 distribution covers the range from 0.01 to 1.76 $R_\odot$ with a mean value of 0.24 $R_\odot$ and a median value

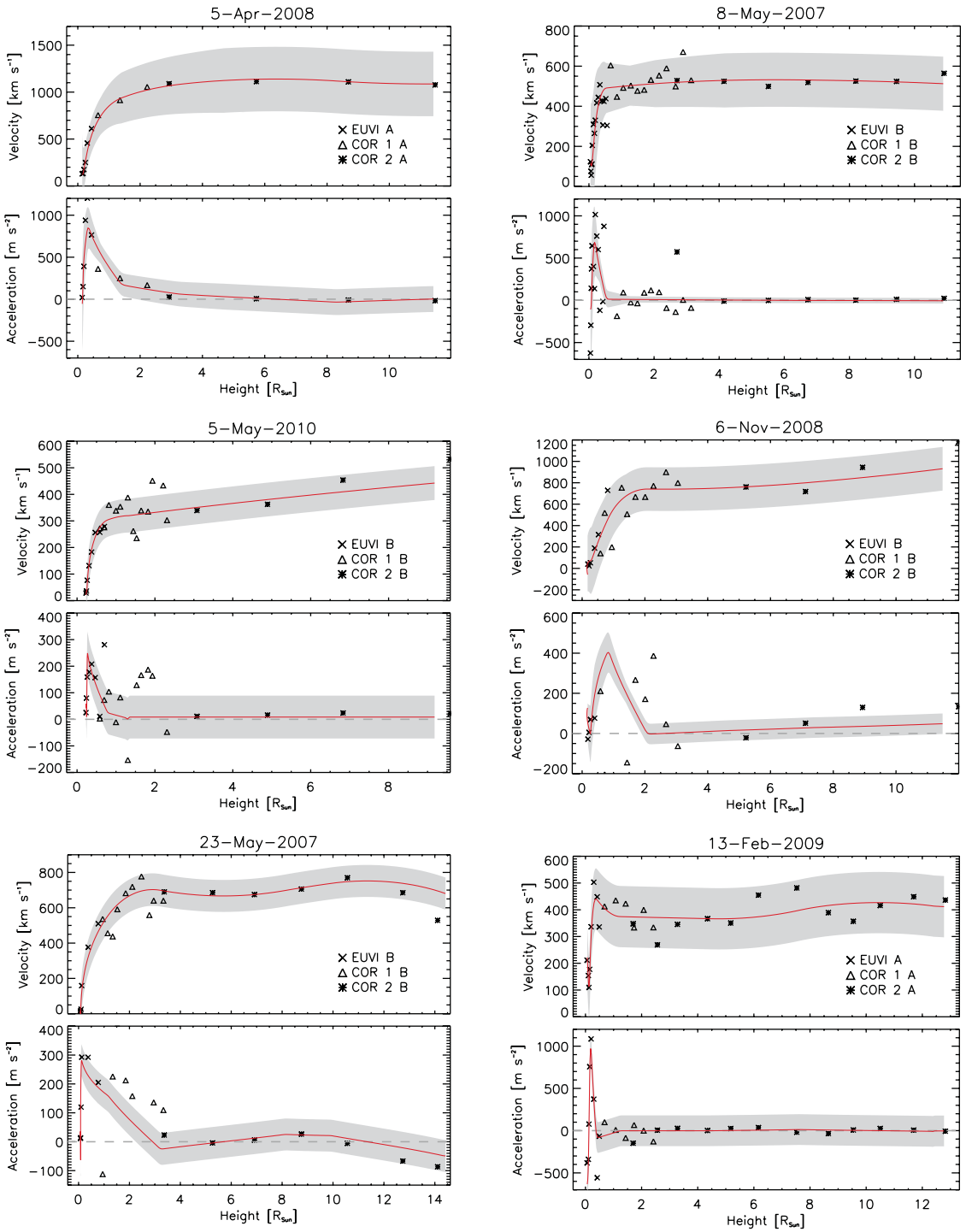

Figure 8. Evolution of the CME velocity and acceleration depending on the CME height for the events occurring on 2008 April 5, 2007 May 8 (top), 2010 May 5, 2008 November 6 (middle), and 2007 May 23 and 2009 February 13 (bottom). Note that the height–time curves of these events are shown in Figures 5–7. The data points derived from the different instruments are marked as crosses (EUVI), triangles (COR1), and asterisks (COR2). The solid lines indicate the first and second derivatives of the spline fits, respectively, which are surrounded by the estimated error range (gray area).

(A color version of this figure is available in the online journal.)

of 0.14 $R_\odot$. The maximum of the distribution is located at the low end at 0.1–0.2 $R_\odot$. The large h_0 values (>0.6 $R_\odot$) are from events that could not be identified in the EUVI FOV but only in coronagraphic images. These may be due to events that really start from source heights $\geqslant$0.6 $R_\odot$ or may be related to observational restrictions in terms of sensitivity for faint CMEs. For our sample of 95 events this applies to 11 CMEs.

The middle panel of Figure 12 shows the distribution of the heights h_{vmax} defined as the velocity values reached at the end of the CME main acceleration phase. The distribution starts at very low heights of 0.17 $R_\odot$ and extends up to 9.5 $R_\odot$ (i.e., close to the border of the COR2 FOV). Sixty-three percent of the events are observed in the range 0–1 $R_\odot$. The mean and median values for h_{vmax} are 1.46 $R_\odot$ and 0.78 $R_\odot$, respectively.

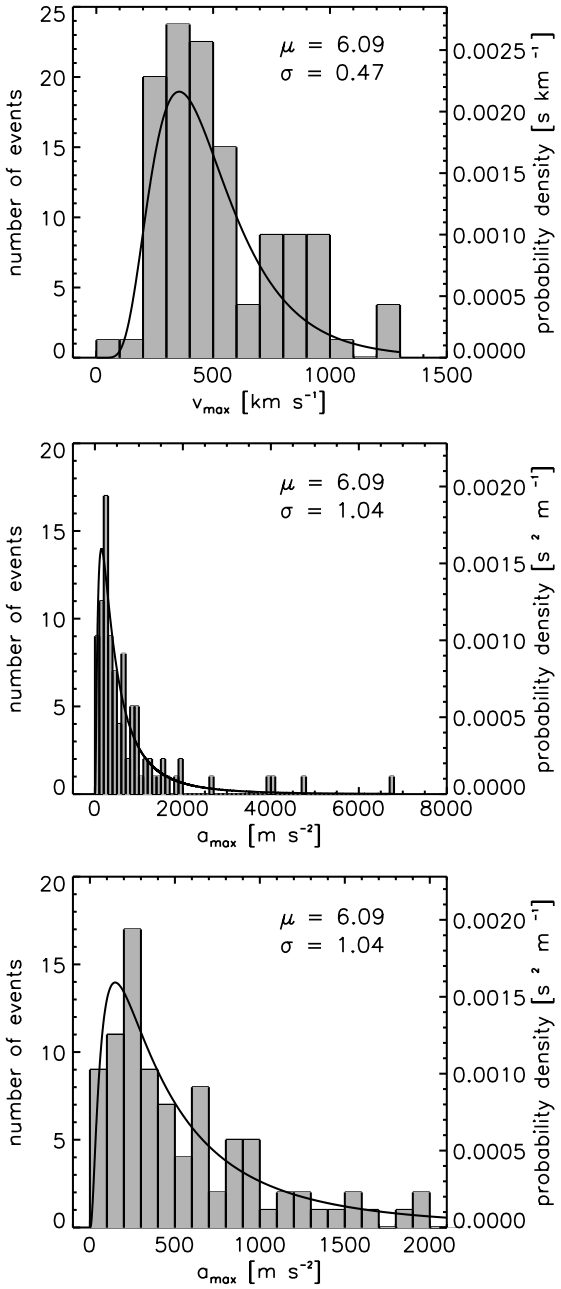

Figure 9. Distribution of the CME peak velocity (top) and peak acceleration (middle) derived for the whole sample of 95 events. The bottom plot shows a zoom of the middle plot restricted to peak accelerations $\leqslant$2000 m s^{-2}. The solid line represents the lognormal fit with μ being the mean and σ being the standard deviation; for details see the main text.

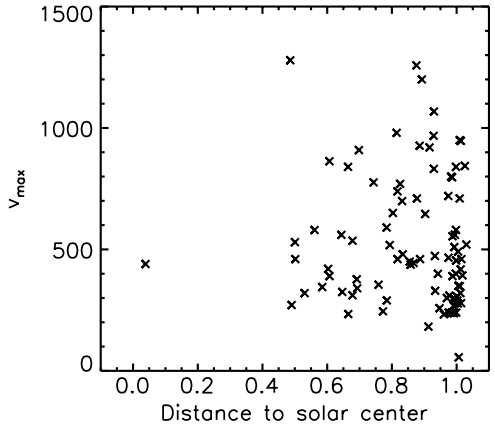

Figure 10. CME peak velocities $v_{\rm max}$ against the projected radial distance to Sun center in units of $R_\odot$.

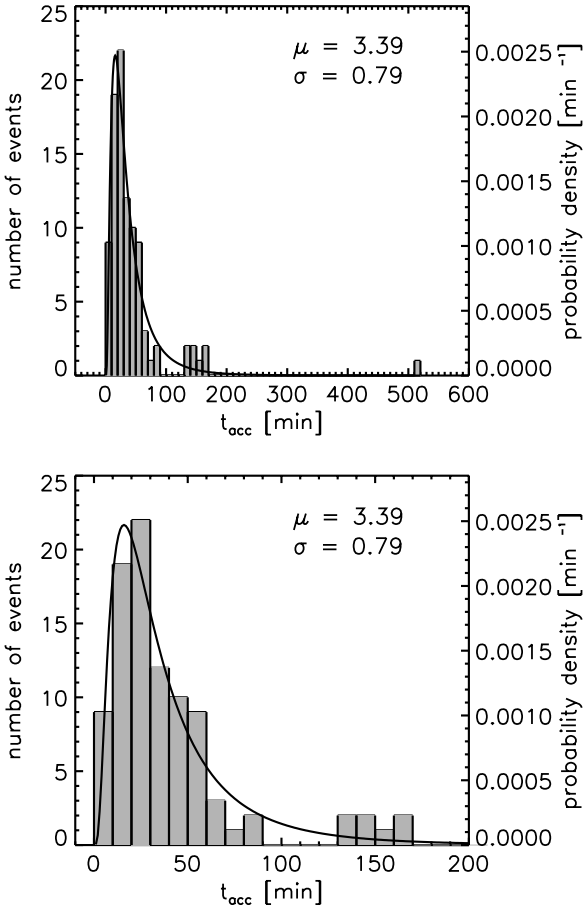

Figure 11. Distribution of CME acceleration duration $t_{\rm acc}$ with a lognormal fit. The bottom plot shows a zoom-in restricted to $t_{\rm acc} < 200$ minutes.

The bottom panel of Figure 12 shows the distribution of the heights $h_{\rm amax}$ at which the CME accelerations reach their maximum. The mean of the $h_{\rm amax}$ distribution is 0.53 $R_\odot$, and the median is 0.26 $R_\odot$. The peak in the $h_{\rm amax}$ distribution lies between 0.2 and 0.3 $R_\odot$, and 74% of the events have $h_{\rm amax}$ smaller than 0.5 $R_\odot$. This means that most of the CMEs studied reach acceleration at very low heights above the solar surface which emphasizes the importance of CME observations in the low corona in order to study the main acceleration phase.

Table 1 gives an overview of all the statistical CME parameters derived: we list the minimum and maximum values, the arithmetic mean with the standard deviation, the median together with the mean absolute deviation (mad), and the two fit parameters of the lognormal fit (μ and σ) for $v_{\rm max}$, $a_{\rm max}$, $t_{\rm acc}$, h_0, $h_{\rm amax}$, and $h_{\rm vmax}$.

In order to identify general characteristics and relationships, which intrinsically describe the evolution of CME eruptions, we correlated the various CME parameters derived. The correlation plots are shown in Figures 13, 15, and 16. All correlations are plotted and calculated in logarithmic space. We found several CME parameters that revealed a significant correlation with CME peak acceleration $a_{\rm max}$. The top panel of Figure 13 shows the scatter plot of $a_{\rm max}$ against $t_{\rm acc}$ revealing a high negative correlation with a correlation coefficient of $c = -0.84$, i.e.,

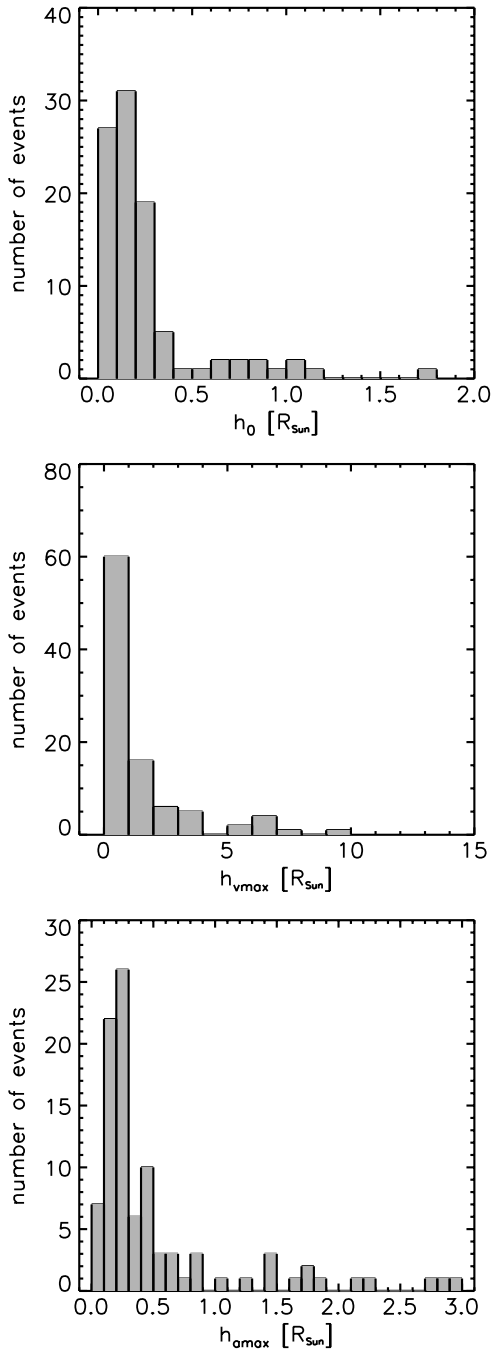

Figure 12. Distribution of h_0, i.e., the height at which the CME front could be first identified (top), height at peak velocity $h_{\rm vmax}$ (middle), and height at peak acceleration $h_{\rm amax}$ (bottom).

CMEs with larger peak accelerations have shorter acceleration durations. This finding fits well with the results obtained in former studies covering smaller CME samples (Zhang & Dere 2006; Vršnak et al. 2007). The slope (−1.09) of the regression line in Figure 13 is in accordance with the results of Vršnak et al. (2007), who found a slope of −1.14. The dependence between $a_{\rm max}$ and $t_{\rm acc}$ can be described with the following power-law relation:[4]

$$a_{\rm max} = 10^{4.23} t_{\rm acc}^{-1.09}. \quad (2)$$

[4] All relations between the different CME parameters are calculated in the same units as used in the scatter plots (Figures 13, 15, and 16), i.e., m s^{-2} for $a_{\rm max}$, km s^{-1} for $v_{\rm max}$, minute for $t_{\rm acc}$, and $R_\odot$ for h_0, $h_{\rm vmax}$, and $h_{\rm amax}$.

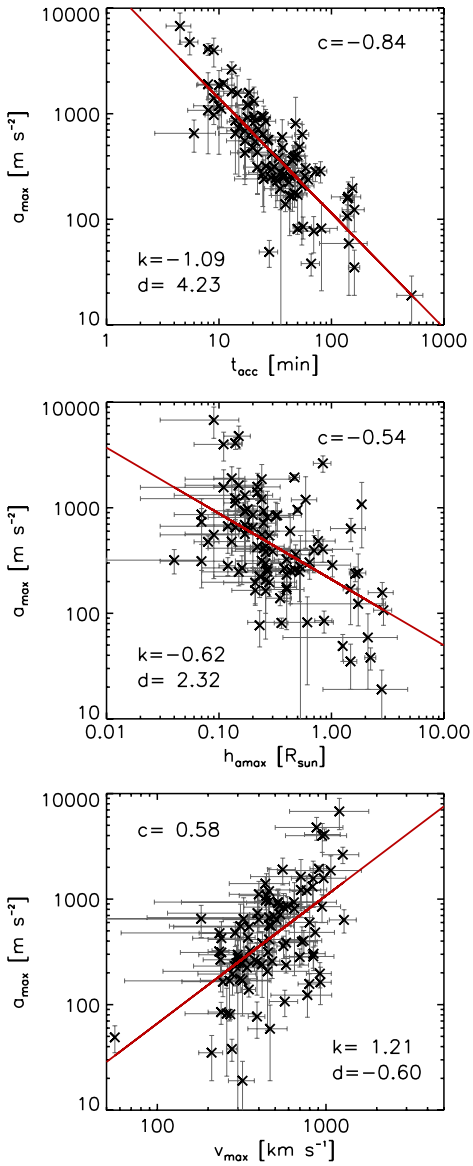

Figure 13. CME peak acceleration against acceleration duration (top), height at peak acceleration (middle), and peak velocity (bottom). The solid lines are linear regression lines to the data points with k being the slope and d being the y-intercept; c gives the correlation coefficient. Note that $a_{\rm max}$, $t_{\rm acc}$, $h_{\rm amax}$, and $v_{\rm max}$ are plotted on a logarithmic scale and that the fits and correlations were also determined in logarithmic space. The same holds for Figures 15 and 16.
(A color version of this figure is available in the online journal.)

The height $h_{\rm amax}$ at which the CME reaches its maximum acceleration and the peak acceleration $a_{\rm max}$ are also anti-correlated, with $c = -0.54$ (Figure 13, middle), i.e., CMEs that are accelerated at lower heights reach higher peak accelerations. Between $a_{\rm max}$ and $h_{\rm amax}$ we found the following dependence:

$$a_{\rm max} = 10^{2.32} h_{\rm amax}^{-0.60}. \quad (3)$$

There is also a distinct correlation between $v_{\rm max}$ and $a_{\rm max}$, $c = 0.58$ (Figure 13, bottom), which is not surprising, since CMEs that have stronger accelerations are also capable of reaching higher peak velocities. Between these two parameters we found the following power-law dependence:

$$a_{\rm max} = 10^{-0.60} v_{\rm max}^{1.21}. \quad (4)$$

Table 1
Statistical CME Parameters Derived

Parameter	Minimum	Maximum	Arithmetic Mean ± Standard Deviation	Median ± Mad	$\mu \pm \sigma$
v_{max} (km s^{-1})	56	1279	526 ± 263	460 ± 160	6.09 ± 0.47
a_{max} (m s^{-2})	19	6781	757 ± 1034	414 ± 246	6.09 ± 1.04
t_{acc} (minute)	4.5	516	44.6 ± 60.4	29.0 ± 14.5	3.39 ± 0.79
h_0 ($R_\odot$)	0.01	1.76	0.24 ± 0.29	0.14 ± 0.08	...
h_{vmax} ($R_\odot$)	0.17	9.5	1.56 ± 1.82	0.78 ± 0.42	...
h_{amax} ($R_\odot$)	0.04	2.90	0.53 ± 0.64	0.26 ± 0.12	...

Notes. Parameters are: Peak Velocity v_{max}, peak acceleration a_{max}, acceleration phase duration t_{acc}, height h_0, where the CME leading edge could be identified for the first time, height at peak velocity h_{vmax}, and height at peak acceleration $h_{amax.}$ The minimum value, maximum value, arithmetic mean with standard deviation, and median with mean absolute deviation (mad) are derived from the whole data set of 95 events. μ and σ are derived from the lognormal fit to the distribution.

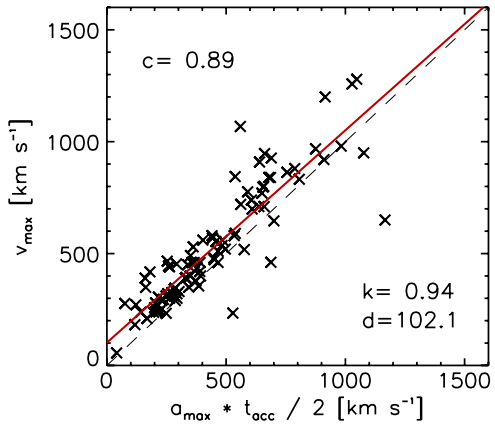

Figure 14. CME peak velocity against the acceleration duration multiplied by half of the peak acceleration, together with the regression line (solid). For comparison the 1:1 correspondence is also plotted (dashed line).
(A color version of this figure is available in the online journal.)

In contrast to the peak accelerations, the CME peak velocities do not show a significant correlation with t_{acc}, h_{vmax}, and h_{amax} (plots not shown).

Figure 14 shows as a test the CME peak velocity v_{max} against $t_{acc}\, a_{max}/2$, which corresponds to modeling the CME acceleration by a triangular profile. We obtain a high correlation coefficient of $c = 0.89$. For comparison, the regression line (solid line) is plotted together with the 1:1 correspondence (dashed line); the two are nearly parallel but shifted against each other by ~0–100 km s^{-1}. This difference can be attributed to a residual acceleration of the CMEs not captured by the simple triangular profile assumed. For the linear regression line we found the following relation:

$$v_{max} = 0.94 t_{acc} \frac{a_{max}}{2} + 102.1, \quad (5)$$

with the same units (km s^{-1}) used on both sides of the equation.

The acceleration duration t_{acc} against h_{vmax} and h_{amax} also shows a power-law dependence with correlation coefficients of $c = 0.76$ and $c = 0.58$, respectively (Figure 15). Their power-law dependence can be written as

$$t_{acc} = 10^{1.51} h_{vmax}^{0.68}, \quad (6)$$

$$t_{acc} = 10^{1.73} h_{amax}^{0.52}. \quad (7)$$

This means that CMEs that accelerate over a longer time also reach their maximum acceleration and velocity at larger heights.

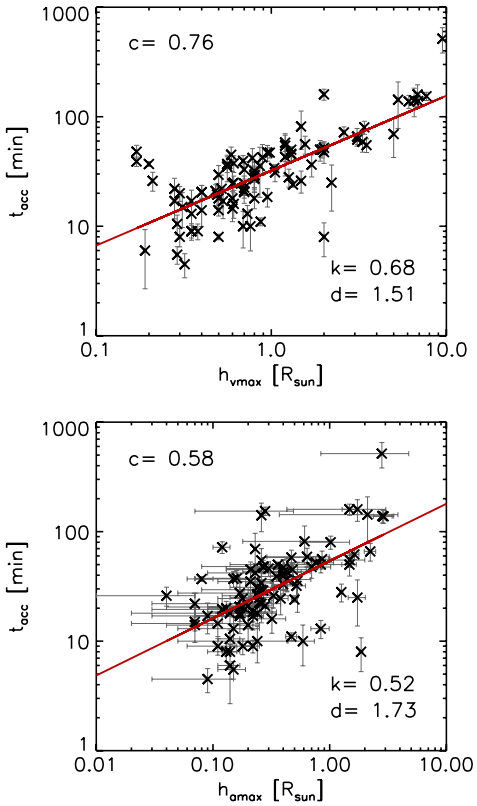

Figure 15. CME acceleration duration against height at peak velocity (top) and height at peak acceleration (bottom).
(A color version of this figure is available in the online journal.)

In Figure 16, we show correlations of the height h_0, at which the CMEs were first observed against h_{amax}, t_{acc}, and a_{max}. A strong correlation between h_0 and h_{amax} is found with a correlation coefficient of $c = 0.82$, i.e., CMEs that start at lower heights also reach their peak acceleration at lower heights. Between h_0 and t_{acc} a weak correlation of $c = 0.43$ is found, i.e., CMEs that originate at low heights tend to accelerate more impulsively. Between h_0 and a_{max} an anti-correlation with $c = -0.46$ was found, i.e., CMEs starting at lower heights in the solar corona reach larger peak accelerations. The relations can be expressed as

$$h_0 = 10^{-0.40} h_{amax}^{0.85}, \quad (8)$$

$$h_0 = 10^{-1.56} t_{acc}^{0.50}, \quad (9)$$

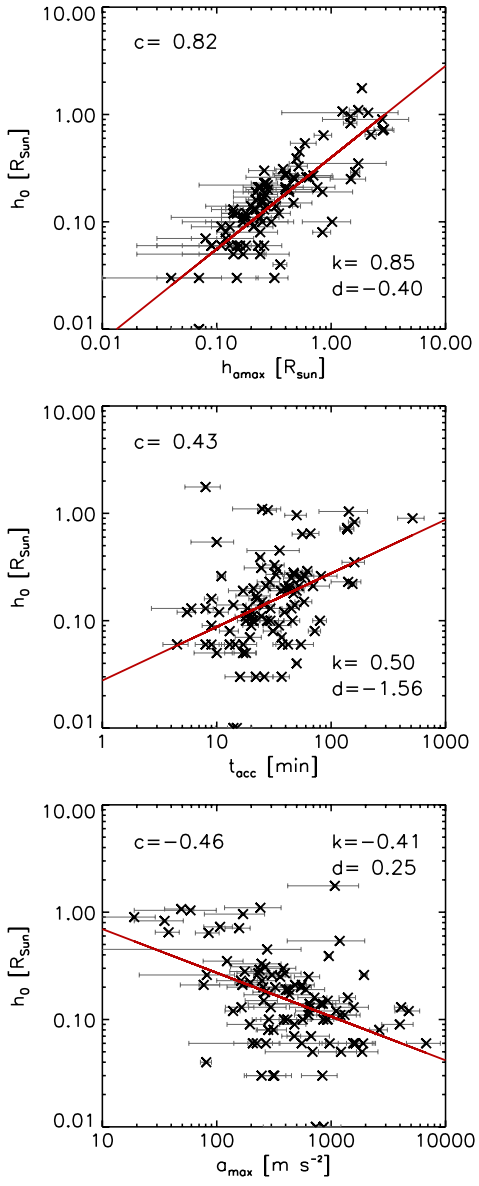

Figure 16. Height h_0 at which the CME front was first detected against the height at peak acceleration (top), acceleration duration (middle), and peak acceleration (bottom).

(A color version of this figure is available in the online journal.)

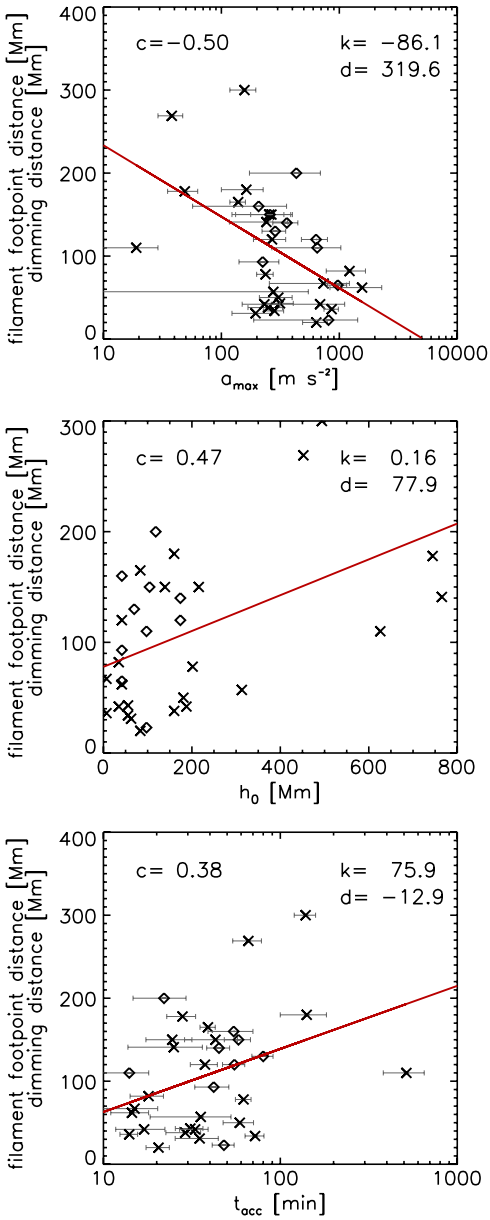

Figure 17. Estimates of the CME source region size against the CME peak acceleration (top), the height of the first CME observation (middle), and acceleration duration (bottom). Crosses indicate the distance of the associated filament footpoints, and diamonds indicate the spatial extent of the coronal dimming region.

(A color version of this figure is available in the online journal.)

$$h_0 = 10^{0.25} a_{\max}^{-0.41}. \quad (10)$$

For 78 out of the 95 events, it was possible to measure at least one feature to estimate the CME source region size. Because there are general differences between the different measurement methods we considered each feature separately. The flare ribbon length of the associated flares did not show any distinct correlation with the CME peak acceleration and velocity but the footpoint distances of the erupting filaments and the size of the coronal dimming did. Figure 17 shows the filament footpoint distances (measured for 24 events) together with the linear extent of the associated coronal dimmings (measured for 10 events) against $a_{\max}$, h_0, and $t_{\rm acc}$. The negative correlation between the source region size L and $a_{\max}$ ($c = -0.50$) and the positive correlation between L and $t_{\rm acc}$ ($c = 0.38$) indicate again that CMEs that originate from compact sources reach higher peak accelerations and have shorter acceleration durations which is consistent with the findings of Vršnak et al. (2007). Between the CME source region size L and initiation height h_0 a positive correlation was found with a correlation coefficient of $c = 0.47$.

5. SUMMARY AND CONCLUSIONS

In the following, we summarize the most important findings of our study based on a sample of 95 impulsive CMEs observed in *STEREO* EUVI, COR1, and COR2.

1. The histograms of the CME peak velocity $v_{\max}$, the CME peak acceleration $a_{\max}$, and the CME acceleration duration $t_{\rm acc}$ can be approximated with a lognormal distribution.
2. We found a wide range of values for $a_{\max}$ (19–6781 m s^{-2}) and $t_{\rm acc}$ (4.5 minutes–8.6 hr).
3. Most of the events (74%) reach their peak acceleration at heights $<0.5\ R_\odot$.

4. a_{max} and t_{acc} are negatively correlated, $c = -0.84$.
5. a_{max} and the height at peak acceleration h_{amax} are negatively correlated, $c = -0.54$.
6. t_{acc} and the height at peak velocity h_{vmax} are positively correlated, $c = 0.76$.
7. t_{acc} and h_{amax} are positively correlated, $c = 0.58$.
8. t_{acc} and the CME initiation height h_0 are positively correlated, $c = 0.43$.
9. h_0 and h_{amax} are positively correlated, $c = 0.82$.
10. h_0 and a_{max} are negatively correlated, $c = -0.46$.
11. The CME source region size L and a_{max} are negatively correlated, $c = -0.50$.
12. L and h_0 are positively correlated, $c = 0.47$.
13. L and t_{acc} are positively correlated, $c = 0.38$.

Based on the assumption that the Lorentz force is the main driver of the eruption, it can be assumed that magnetic energy is transformed into kinetic energy and thus

$$\frac{\rho v^2}{2} \leqslant \frac{B^2}{2\mu_0} \tag{11}$$

or

$$v < \left(\frac{B^2}{\mu_0 \rho}\right)^{1/2} = v_A, \tag{12}$$

with B being the magnetic field strength within the CME body, μ_0 being the magnetic permeability in vacuum, v_A being the Alfvén velocity, ρ being the plasma density, and v being the CME velocity. Equation (12) states that the CME velocity cannot be larger than the Alfvén velocity in the erupting structure (e.g., Vršnak 2006).

The Lorentz force density can be expressed as

$$\boldsymbol{f} = \boldsymbol{j} \times \boldsymbol{B} = \frac{1}{\mu_0}\left[(\boldsymbol{B}\cdot\boldsymbol{\nabla})\boldsymbol{B} - \boldsymbol{\nabla}\left(\frac{\boldsymbol{B}^2}{2}\right)\right] \tag{13}$$

with $\boldsymbol{j}$ being the current density. Inserting the approximation $\boldsymbol{\nabla} \approx 1/L$, we obtain the following order of magnitude estimate (see also Vršnak et al. 2007):

$$a < \frac{B^2}{2\mu_0 \rho L} = \frac{v_A^2}{2L} \tag{14}$$

with L being the characteristic length scale over which the magnetic field varies, which can be approximated by the CME source region size. Equation (14) shows that the acceleration is not only governed by the Alfvén velocity but is also dependent on the size of the erupting structure. Initially compact CMEs (small L, large v_A) will reach higher accelerations. These considerations coincide with our observational findings (summary items 10 and 11), i.e., the inverse proportionality found between a_{max} and L (Figure 17, top) and also a_{max} and h_0 (Figure 16, bottom), which can be used as an alternative estimate of the source region size. We tested the relation between the CME peak acceleration, the size of the erupting flux rope, and the Alfvén velocity implied by Equation (14), in that we derived for each event the ratio $v_{max}^2/(2L)$ and $v_{max}^2/(2h_0)$ (with $v_{max} < v_A$; see Equation (12)) and correlated these quantities with a_{max}. The resulting correlation coefficients lie in the range of 0.6–0.7 (Figure 18), i.e., they are higher than the correlations of the individual CME parameters, which supports our interpretation.

The distinct anti-correlation found between h_0 and a_{max} with $c \sim -0.5$ is also related to the stronger magnetic fields in the lower corona, which in turn are related to larger Lorentz forces providing the driving force for the CME acceleration. We note that we interpret the parameter h_0, defined as the height where a CME is first observed, to be a measure of the initiation height of the erupting CME (and thus, to some extent, also to be a measure of the original size of the erupting structure). This is of course somewhat critical, since in gradual and faint CMEs we expect that we cannot really observe a CME from its very initiation site (due to the limited sensitivity) but only further out when sufficient mass is accumulated at the CME front to be observable. Indeed, in 11 out of 95 events we could not find signatures of the erupting CME in the EUVI but only in the COR1 FOV. This may be a real effect, i.e., some CMEs in our sample started at heights $\gtrsim 0.7\ R_\odot$, but it may also be partly biased by the fact that the CME actually started at lower heights but was too faint to be observed. However, even if we underestimated the CME initiation height by using the height h_0 where the CME was first observed, the distinct correlations that we obtained between h_0 and other characteristic CME quantities such as a_{max}, v_{max}, and t_{acc}, in line with the interpretations in terms of the Lorentz force elaborated above, support it being a very useful quantity for CME initiation studies.

Since during its propagation the size of a CME increases with height, we also expect from Equation (14) that the acceleration decreases with height. This is consistent with our findings of a distinct anti-correlation between a_{max} and h_{amax} (summary item No. 5; see also the bottom panel of Figure 13). The distinct inverse proportionality that we derived between a_{max} and t_{acc} (summary item No. 4; see the top panel of Figure 13) explains the relative small range of CME velocities (one order

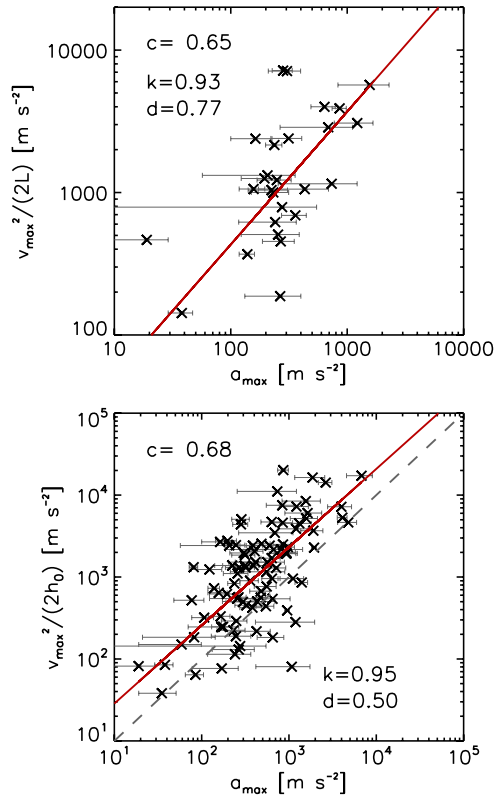

Figure 18. Top: relation of Equation (14) to the CME source region size L (filament footpoint distance, dimming extent). Bottom: same relation but with the height h_0 at which the CME was first observed instead of L.

(A color version of this figure is available in the online journal.)

of magnitude) despite the large ranges over which $a_{\max}$ (two orders of magnitude) and $t_{\rm acc}$ (three orders of magnitude) vary.

Taking into account that the acceleration time cannot be shorter than the Alfvén wave signal transit time, we get the order-of-magnitude relation

$$t_{\rm acc} \geqslant \frac{2L}{v_A}, \tag{15}$$

i.e., CMEs originating from compact sources accelerate more impulsively, consistent with our summary item No. 13 (Figure 17, bottom) and No. 8 (Figure 16, top), where we interpret h_0 as another measure of the source region size.

The distributions of the CME peak velocity, CME peak acceleration, and acceleration duration show a lognormal behavior (summary item No. 1). Such distributions are created by the product of several independent variables. We suggest that the energy of the CME is dependent on at least two major variables. On the one hand, it depends on the amount of initially stored magnetic energy, which is available for transformation into other forms of energy. Furthermore, the CME energy also depends on the "transmission coefficient," i.e., the percentage of the initially stored energy that will be transformed into kinetic energy of the CME.

This work was supported by the Österreichische Förderungsgesellschaft (FFG) of the Austrian Space Applications Programme (ASAP) under grant No. 819664 and by the Austrian Science Fund (FWF): P20867-N16. The European Community's Seventh Framework Programme (FP7/2007-2013) under grant agreement No. 218816 (SOTERIA) is acknowledged by B.V. We thank the anonymous referee for insightful comments which helped to improve the paper. The *STEREO*/SECCHI data are produced by an international consortium of the Naval Research Laboratory (USA), Lockheed Martin Solar and Astrophysics Lab (USA), NASA Goddard Space Flight Center (USA), Rutherford Appleton Laboratory (UK), University of Birmingham (UK), Max-Planck-Institut für Sonnensystemforschung (Germany), Centre Spatiale de Liège (Belgium), Institut d'Optique Théorique et Appliquée (France), and Institut d'Astrophysique Spatiale (France).

REFERENCES

Cheng, X., Zhang, J., Ding, M. D., & Poomvises, W. 2010, ApJ, 712, 752
Gallagher, P. T., Lawrence, G. R., & Dennis, B. R. 2003, ApJ, 588, L53
Gopalswamy, N., Lara, A., Lepping, R. P., et al. 2000, Geophys. Res. Lett., 27, 145
Gopalswamy, N., Yashiro, S., Michalek, G., et al. 2009, Earth Moon Planets, 104, 295
Howard, R. A., Moses, J. D., Vourlidas, A., et al. 2008, Space Sci. Rev., 136, 67
Kaiser, M. L., Kucera, T. A., Davila, J. M., et al. 2008, Space Sci. Rev., 136, 5
Limbert, E., Stahel, A. W., & Abbt, M. 2001, Bioscience, 51, 341
Maričić, D., Vršnak, B., Stanger, A. L., & Veronig, A. 2004, Sol. Phys., 225, 337
Morgan, H., Habbal, S. R., & Woo, R. 2006, Sol. Phys., 236, 263
Schwenn, R., dal Lago, A., Huttunen, E., & Gonzalez, W. D. 2005, Ann. Geophys., 23, 1033
Temmer, M., Veronig, A. M., Kontar, E. P., Krucker, S., & Vršnak, B. 2010, ApJ, 712, 1410
Temmer, M., Veronig, A. M., Vršnak, B., et al. 2008, ApJ, 673, L95
Vourlidas, A., Howard, R. A., Esfandiari, E., et al. 2010, ApJ, 722, 1522
Vršnak, B. 2006, Adv. Space Res., 38, 431
Vršnak, B., Maričić, D., Stanger, A. L., et al. 2007, Sol. Phys., 241, 85
Wuelser, J., Lemen, J. R., Tarbell, T. D., et al. 2004, Proc. SPIE, 5171, 111
Yashiro, S., Gopalswamy, N., Michalek, G., et al. 2004, J. Geophys. Res. (Space Phys.), 109, 7105
Yurchyshyn, V., Yashiro, S., Abramenko, V., Wang, H., & Gopalswamy, N. 2005, ApJ, 619, 599
Zhang, J., & Dere, K. P. 2006, ApJ, 649, 1100
Zhang, J., Dere, K. P., Howard, R. A., Kundu, M. R., & White, S. M. 2001, ApJ, 559, 452
Zhang, J., Dere, K. P., Howard, R. A., & Vourlidas, A. 2004, ApJ, 604, 420